Bioactive Materials 14 (2022) 31–41

Contents lists available at ScienceDirect

Bioactive Materials

journal homepage: www.keaipublishing.com/en/journals/bioactive-materials

A nanoconcrete welding strategy for constructing high-performance wound dressing

Yingshuai Wang [a,b,c,1], Yanxia Zhu [c,1], Penghe Zhao [c], Bin Wei [d], Mingjian Fan [c], Danyang Chen [c,e], Zhaokui Jin [c], Qianjun He [b,c,e,*]

[a] School of Life Science and Technology, Weifang Medical University, Weifang, Shandong, China
[b] Central Laboratory, Longgang District People's Hospital of Shenzhen & the Third Affiliated Hospital (Provisional) of the Chinese University of Hong Kong, Shenzhen, Guangdong, China
[c] School of Biomedical Engineering, Health Science Center, Shenzhen University, No. 1066 Xueyuan Road, Shenzhen, 518060, Guangdong, China
[d] Department of Quantum and Energy Materials, International Iberian Nanotechnology Laboratory (INL), Braga, 4715-330, Portugal
[e] Center of Hydrogen Science, Shanghai Jiao Tong University, Shanghai, 200240, China

ARTICLE INFO

Keywords:
Tissue engineering
Mechanical performances
Calcium carbonate
Mesoporous materials
Organic/inorganic nanocomposite
Wound dressing

ABSTRACT

Engineering biomaterials to meet specific biomedical applications raises high requirements of mechanical performances, and simultaneous strengthening and toughening of polymer are frequently necessary but very challenging in many cases. In this work, we propose a new concept of nanoconcrete welding polymer chains, where mesoporous $CaCO_3$ ($mCaCO_3$) nanoconcretes which are composed of amorphous and nanocrystalline phases are developed to powerfully weld polymer chains through siphoning-induced occlusion, hydration-driven crystallization and dehydration-driven compression of nanoconcretes. The $mCaCO_3$ nanoconcrete welding technology is verified to be able to remarkably augment strength, toughness and anti-fatigue performances of a model polymer poly(3-hydroxybutyrate-*co*-3-hydroxyvalerate)-based porous membrane. Mechanistically, we have revealed polymer-occluded nanocrystal structure and welding-derived microstress which is much stronger than interfacial Van der Waals force, thus efficiently preventing the generation of microcracks and repairing initial microcracks by microcracks-induced hydration, crystallization and polymer welding of $mCaCO_3$ nanoconcretes. Constructed porous membrane is used as wound dressing, exhibiting a special nanoplates-constructed surface topography as well as a porous structure with plentiful oriented, aligned and opened pore channels, improved hydrophilicity, water vapor permeability, anti-bacterial and cell adherence, in support of wound healing and skin structural/functional repairing. The proposed nanoconcrete-welding-polymer strategy breaks a new pathway for improving the mechanical performances of polymers.

1. Introduction

Mechanical and biological performances are two key indicators for engineering biomaterials such as bone-implant biomaterials, wound dressing and artificial skin, which often need relatively high strength, toughness and bioactivity [1,2]. Many promising polymers and bioceramics with high biocompatibility have to be strengthened and/or toughened to meet the demands of clinical applications. One of the classic methods for strengthening and toughening is to incorporate second-phase nanoparticles in the matrix [3–8]. The interfacial attraction between nanoparticle and polymer chain is the key to block microcrack for toughening. However, the interfacial attractions, including Van der Waals forces, hydrogen bonding and electrostatic pull, are relatively weak and generally lower than the attraction between polymer crystal grains, leading to the limited toughening outcomes and even strength loss. It is a great challenge for simultaneous strengthening and toughening in many cases. In addition, the favorable composition and surface topography of polymer-based composites can endow them with a specific anti-bacterial capability in support of tissue engineering, which can be modulated by incorporating active

Peer review under responsibility of KeAi Communications Co., Ltd.
* Corresponding author. Central Laboratory, Longgang District People's Hospital of Shenzhen & the Third Affiliated Hospital (Provisional) of the Chinese University of Hong Kong, Shenzhen, Guangdong, China.
E-mail address: nanoflower@126.com (Q. He).
[1] These authors made equal contribution to this work.

https://doi.org/10.1016/j.bioactmat.2021.12.014
Received 29 September 2021; Received in revised form 14 November 2021; Accepted 1 December 2021
Available online 18 December 2021

components and inorganic nanomaterials [9–11]. To construct such favorable composition and surface topography is vitally important.

$CaCO_3$ nanoparticle as a second-phase incorporation material has been well applied in the plastics industry owing to its high availability, low cost and high whiteness, and also exhibits a high potential for biomedical application because of its high biocompatibility and biodegradability [12,13]. However, popular methods of modifying polymers with $CaCO_3$ nanoparticles still depend on weak interfacial attraction. It is worth noticing that amorphous $CaCO_3$ exhibits polymer-like flexibility, enabling it to copolymerize with polymers and also to encapsulate micelles, carbon nanodots, gold nanoparticles, macromolecules, small-molecule amino acids and fluoresceins during its crystallization [13–25]. Therefore, we here hypothesize that powerfully welding polymer chains within $CaCO_3$ nanocrystal through siphoning-induced occlusion, hydration-driven crystallization and dehydration-driven compression of amorphous mesoporous $CaCO_3$ nanoconcretes will possibly more effectively enhance the strength and toughness of the polymer. However, it is challenging to prepare

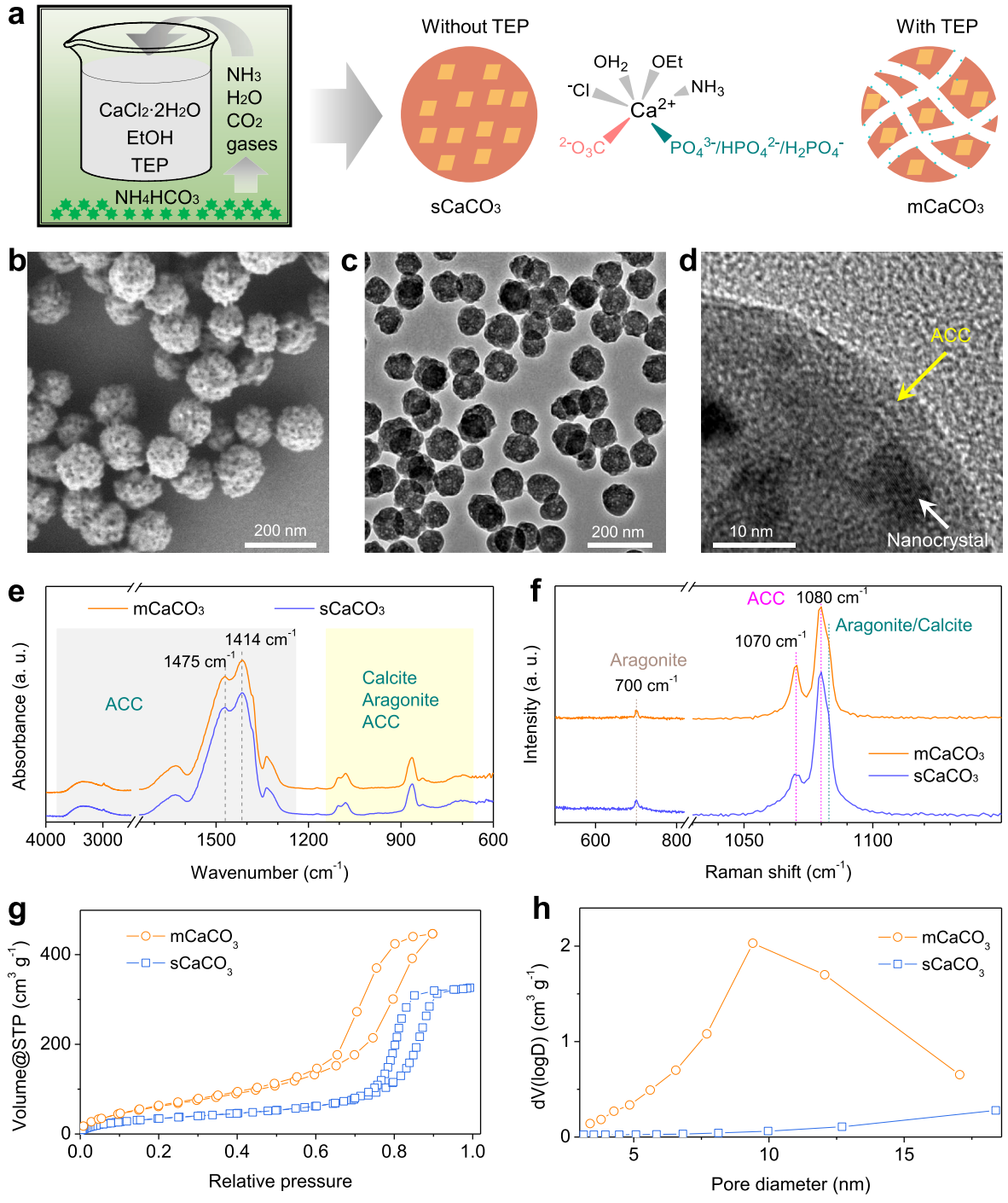

Fig. 1. Synthesis and characterization of $CaCO_3$ nanoconcretes. (**a**) Schematic illustration of the synthesis of $sCaCO_3$ and $mCaCO_3$ nanoconcretes, (**b**) Scanning electronic microscopy (SEM) image of $mCaCO_3$ nanoconcretes, (**c**) Transmission electron microscope (TEM) image of $mCaCO_3$ nanoconcretes, (**d**) High-resolution TEM image of $mCaCO_3$ nanoconcretes, (**e**) FT-IR spectra, (**f**) Raman spectra, (**g**) N_2 adsorption-desorption curves, and (**h**) pore diameter distributions of $sCaCO_3$ and $mCaCO_3$ nanoconcretes.

amorphous mesoporous $CaCO_3$ nanoparticles as it has not been reported previously.

In this work, we developed an ion-etching method to synthesize a new type of mesoporous $CaCO_3$ nanoconcretes ($mCaCO_3$) composed of amorphous and nanocrystalline $CaCO_3$ (Fig. 1a), and then constructed a kind of porous membrane by $mCaCO_3$ welding poly(3-hydroxybutyrate-*co*-3-hydroxyvalerate) (PHBV) by a freeze-drying/hydration method (Fig. 2a). The as-constructed porous membrane exhibited remarkably augmented strength, toughness and anti-fatigue performances. Proof-of-concept experimental results verified our hypothesis that the welding of polymer chains with $mCaCO_3$ made primary contributions to simultaneous strengthening and toughening of polymer. Polymer chains (the welding object) were adsorbed within the porous channels of mesoporous $CaCO_3$ nanoparticles ($mCaCO_3$, the welding node) which were composed of amorphous and nanocrystalline phases, and then clamped/welded by the dehydration-driven mechanical force during the crystallization of $mCaCO_3$, forming a kind of $mCaCO_3$-polymer occlusion. The constructed porous membrane as wound dressing also demonstrated a special nanoplates-constructed surface topography in favor of antibacterial and promoted epithelial cell adherence and proliferation, plentiful oriented, aligned and opened pore channels (about 100 nm in diameter) in favor of improved hydrophilicity and water vapor permeability, together in support of wound repairing.

2. Materials and methods

2.1. Chemicals and reagents

Calcium chloride dihydrate ($CaCl_2 \cdot 2H_2O$), triethyl phosphate (TEP), ammonium bicarbonate (NH_4HCO_3) and rhodamine B (RhB) were purchased from Sigma-Aldrich. All other reagents used were of the highest commercial grade available. Cell Counting Kit-8 (CCK-8) and calcein-AM were purchased from Beyotime Biotechnology Co., Ltd. Pure water was produced from a Milli-Q Academic Water Purification System (Millipore Corp., Billerica, MA, USA). Mouse 3T3 fibroblast cells were purchased from Shanghai Zhong Qiao Xin Zhou Biotechnology Co., Ltd.

2.2. Preparation and characterization of $mCaCO_3$ and $sCaCO_3$ nanoparticles

A modified gas diffusion method was used to prepare $mCaCO_3$ and $sCaCO_3$. At first, $CaCl_2 \cdot 2H_2O$ (5 mM) and TEP (3 mM) were dissolved in 40 mL anhydrate ethanol in a fresh and smooth glass bottle, which was sealed with parafilm with five pinholes. The bottle was put in a container, and then a plentiful amount of NH_4HCO_3 powder was evenly paved outside the bottle at the bottom of the container, and finally the container was sealed. After static incubation at room temperature for 7 days, the product $mCaCO_3$ was collected by centrifugation, and washed with anhydrate ethanol for 3 times, and then freshly used for the preparation of porous membrane. $sCaCO_3$ was synthesized by a similar

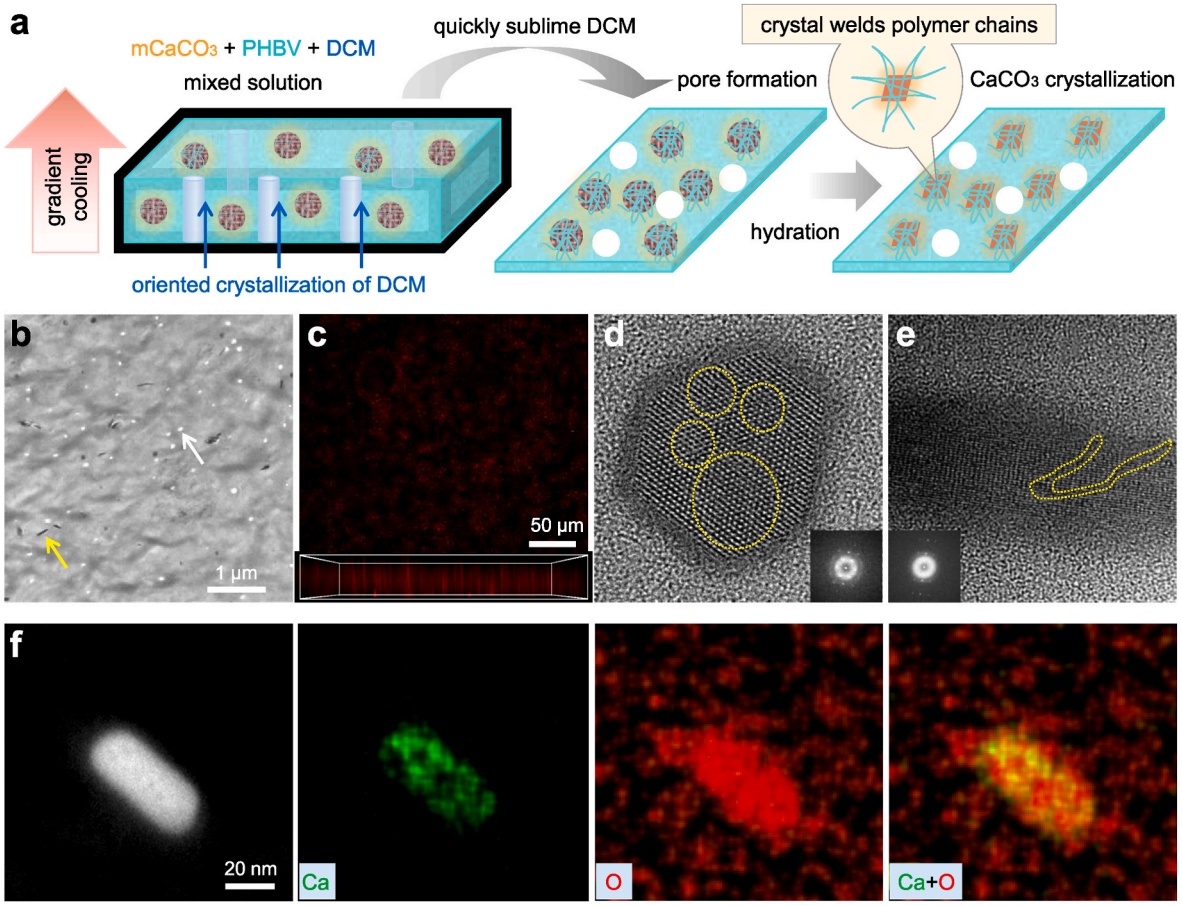

Fig. 2. Preparation and characterization of porous $mCaCO_3$-PHBV membranes. (**a**) Schematic diagram of the preparation of $mCaCO_3$-PHBV membrane, (**b**) TEM image of a 60 nm-thick slice of $mCaCO_3$-PHBV membrane where white and yellow arrows point to pore and calcite nanocrystal respectively, (**c**) Two-photon confocal microscope image of $mCaCO_3$-PHBV membrane after pores were stained with rhodamine B (above inset, top view; below inset, side 3D view), (**d**,**e**) High-resolution TEM images of calcite nanocrystals in the 60 nm-thick slice of $mCaCO_3$-PHBV membrane where yellow dashed circles represent intracrystal deficiencies and corresponding selected area electron diffraction (SEAD) images (the inset), (**f**) HADDF image and corresponding elementary mapping of the 60 nm-thick slice of $mCaCO_3$-PHBV membrane.

method in the absence of TEP.

The morphologies and sizes of $mCaCO_3$ and $sCaCO_3$ were observed on scanning electron microscopes (Apero/Nova NanoSEM, FEI) and on a transmission electron microscope (Tecnai TF20, FEI). The composition was detected by Fourier transform infrared spectroscopy (Nexus 670, Thermo-Nicolet), Raman spectroscopy (Renishaw inVia Raman Microscope), X-ray diffraction (Ultima IV, Rigaku). The content of water was measured by thermogravimetric analysis (TGA) using a thermogravimetric analyzer (Q200, TA).

2.3. Preparation and characterization of porous membranes

Porous membranes were prepared by a freeze-drying method. PHBV (75 mg) was fully dissolved in dichloromethane (DCM, 3 mL), and $CaCO_3$ nanoparticles (15 mg) were thoroughly dispersed into the above solution. The mixture solution was poured into a home-made smooth stainless steel mold (7 cm × 3 cm × 3 cm) which was wrapped with tin foil and then put into a heat preservation box to keep on the horizon. A plentiful amount of liquid nitrogen was quickly poured into the box to freeze the polymer solution. The mold-contained box was rapidly transferred to a constant temperature vacuum drying oven to vacuumize the membrane for 30 min and then maintain vacuum overnight in order to completely remove DCM. Finally, the porous membrane was pulled off from the mold carefully, and then immersed into deionized water for 2 days. Water on the surface of the porous membrane was drained dry and then as-prepared porous membranes were stored for use. A bigger dimension of mold (20 cm × 20 cm × 5 cm) was also made to prepare a big area of the porous membrane without quality loss.

The surface microstructure patterns of porous membranes were observed on a scanning electron microscope (Apero, FEI). As to microstructure measurement, porous membranes were embedded into resin, and then cut into 60 nm-thick membranes to put on glass sheets or TEM copper meshes for various measurements. High-resolution TEM images and elementary mapping were collected using HT7700 (Hitachi) and Titan Cubed Themis G2 300 (FEI). Contact angles of porous membranes were measured on a Dynamic Contact Angle Meter (XG-CAMC, Shanghai Xuanzhun Instrument Co., Ltd.).

2.4. 3D fluorescence imaging of pore structure of porous membrane

Dry porous membrane was immersed in an ethanol solution of RhB to be vacuumized for 2 h. Residual RhB on the surface of the porous membrane was washed away with ethanol. After oil seal on a glass sheet, a three-dimensional structure of the porous membrane was scanned layer by layer on a two-photon confocal laser scanning microscope (ZEISS LSM880) and then reconstructed.

2.5. Measurement of mechanical performances

The porous membrane was cut into a strip with a standard dimension of 15 cm × 5 cm, and then fixed with a clamp at an equal distance on both ends. Tensile measurement was executed at a stretch speed of 5 mm/min on a UTM2012 high-resolution universal tensile testing machine (Shenzhen Henwiton Electronic Technology Co., Ltd.) with a sampling frequency of 120 Hz by a multi-channel synchronic data collection mode, and stopped until porous membrane was completely broken. As for anti-fatigue bending measurement, the porous membrane was bent 3 mm in the vertical distance and then unfolded for location recovery at a speed of 30 mm/min for 500 cycles on the universal tensile testing machine. At the maximal bending strength, a circularly bent porous membrane was used to measure its maximal tensile strength.

2.6. Measurement of the permeability of porous membranes

The water vapor permeability of porous membranes was measured by the differential-pressure method. A round-mouth glass bottle was filled with water and then sealed with porous membranes to achieve an effective transmission area of 1.54 cm^2. The bottle was placed in a vacuum drying oven to maintain at 1 atm at 25 °C for 5 h, and then weighted water loss to calculate the water vapor transmission.

2.7. Antibacterial performance measurement

Escherichia coli and *Staphylococcus aureus* were cultured to log phase (10^8 CFU/mL) and diluted 1,000 times to prepare bacterial suspensions in LB liquid medium. Porous membranes were cut into discs with 5 mm in diameter by a hole punch and put in a 96-well plate ($n = 6$). A diluted bacterial suspension was added into wells (100 μL/well), and then incubated at 37 °C for 24 h. The absorbance at 600 nm was measured on a microplate reader (Synergy H1M, Bio-Tek) to determine bacterial concentration.

2.8. Measurement of cytotoxicity and cell proliferation

As to cytotoxicity measurement, a 5 mm-diameter circular disk of the porous membrane ($n = 6$) was put in the well of 96-well plates after sterilization, and then 10^4 3T3 cells or MCF-10A cells were added into each well. After incubation at 37 °C under an atmosphere of 5% CO_2 and 90% relative humidity in an incubator (Thermo Scientific) for 24 h, CCK-8 reagent was used to detect the absorbance at 450 nm using the Bio-Tek microplate reader and then to calculate cytotoxicity by subtracting the background prior to the addition of CCK-8.

As for cell adherence and proliferation measurement, a 1.5 cm-diameter circular disk of the porous membrane was placed in a 12-well plate after sterilization, and then 4×10^3 3T3 cells were added into each well. Culture medium was replaced with a fresh one once 48 h. After continuous culture for 7 days, porous membranes were taken out, and un-adhered cells were washed away with PBS gently and then stained with calcein-AM for fluorescence observation (488 nm/515 nm as excitation/emission wavelengths) on a confocal laser scanning microscope (TCS SP5 II).

2.9. Animal experiments

About 4-week old female BALB/c mice (~20g, purchased from Guangdong Medical Laboratory Animal Center) were randomly divided into four groups ($n = 12$), Control, PHBV, $sCaCO_3$@PHBV, and $mCaCO_3$-PHBV. After anesthetization by intraperitoneal injection 100 μL of 10% chloral hydrate and subsequent removal of the hair on the back, a 1 cm-diameter wound was created using a special hole punch to remove the whole cortex on a sterile operation platform. After being stuck with a porous membrane as wound dressing, the wound was wrapped with gauze and bandage, and then observed at Day 1, 5, 7, 10, and 13, respectively. After treatment for 13 days, mice were humanely sacrificed, and then the skin on healed wound was removed and fixed with 4% paraformaldehyde, and then the slice of the healed skin at the center of the wound was stained by H&E and Masson methods for histological analysis. In addition, several main organs (heart, liver, spleen, lung and kidney) were collected, fixed with 4% paraformaldehyde, and stained with H&E for histological analysis. Moreover, Before humane execution after 13 day treatment, the blood of each mouse was collected and then used for assessment of liver/kidney functions and hemotoxicity on a biochemical analyzer (iMagic-M7) and a blood cell analyzer (BC–31S, Mindray).

3. Results and conclusion

3.1. Synthesis and characterization of $CaCO_3$ nanoconcretes

A classical gas diffusion method was used to synthesize $CaCO_3$ nanoconcretes using $CaCl_2{\cdot}2H_2O$ as calcium/water sources and NH_4HCO_3 as carbonate/water sources (Fig. 1a). In order to obtain stable

amorphous $CaCO_3$ nanoparticles, ethanol was used as the solvent instead of water because it is hard for them to stabilize in an aqueous solution. Moreover, ethanol has a relatively lower dielectric constant (24.5) than water (78.5), and can therefore confine the dissociation/ionization of all reactants, reducing reaction rate in favor of controllable uniform growth of $CaCO_3$ nanoparticles. In this system, additive water except $CaCl_2{\cdot}2H_2O$ and NH_4HCO_3 will easily lead to unwanted $CaCO_3$ crystallization. Ethanol, H_2O, Cl^- and NH_4^+ all can coordinate with Ca^{2+} and consequently inhibit $CaCO_3$ precipitation together in support of controlled growth with about 3 days of the incubation period for visible precipitation [26]. Unexpectedly, we found from IR (Fig. 1e), Raman (Fig. 1f), XRD (Supplementary Fig. S1) and TEM (Supplementary Fig. S2) measurements that the synthesized $CaCO_3$ nanoparticles were a mixture of amorphous calcium carbonate (ACC), aragonite and calcite nanocrystals, which was rarely observed previously, although similar $CaCO_3$ nanoparticles were synthesized under similar conditions by the same method by many other researchers [27–31]. In addition, collected solid $CaCO_3$ ($sCaCO_3$) nanoconcretes can be recrystallized into submicron calcite crystals by the hydration and dehydration evolution when transferred to an aqueous solution (Supplementary Fig. S3). Such a mixture structure and a consolidation behavior are quite similar to that of concrete, and therefore we called them nanoconcretes in this work.

Furthermore, we attempted to add etchants to obtain a porous structure of $CaCO_3$ nanoconcretes. Triethyl phosphate (TEP) was selected as an etching agent because its hydrolysis products phosphates are a poison able to effectively inhibit $CaCO_3$ precipitation by highly competing with carbonate ions for coordination with Ca^{2+} (Fig. 1a) as calcium carbonate normally does not precipitate from phosphates-rich seawater with 300% supersaturation [32–34]. From SEM and TEM images (Fig. 1bc and Supplementary Fig. S4), we can clearly find that $CaCO_3$ nanoconcretes which were synthesized in the presence of TEP had high porosity (mesoporous $CaCO_3$ nanoconcretes, $mCaCO_3$). Moreover, from Brunauer-Emmett-Teller (BET) measurement results (Fig. 1gh), $mCaCO_3$ exhibited an obvious mesoporous structure with porous size of 2–20 nm (about 10 nm in average pore size) and higher specific surface area (417 cm^2/g) compared with $sCaCO_3$ (81 cm^2/g) in accordance with the above SEM observation results. From TG results (Supplementary Fig. S5), we further found that the water content of mesoporous $CaCO_3$ nanoconcretes ($mCaCO_3$) was lower than that of the above-mentioned solid $CaCO_3$ nanoconcretes ($sCaCO_3$), indicating that $mCaCO_3$ had a higher proportion of ACC, owing to stronger inhibition effect of phosphates against aragonite and calcite crystals. The environment-sensitive buffered system can induce the dissolution-reprecipitation evolution during gas diffusion [35–37], which was possibly the main reason that phosphates can drill pores in the ACC phase. A dilute ethanol solution of water (volume ratio of water to ethanol = 5:95) was used to check the phase transformation behavior of $mCaCO_3$, which experienced a phase transformation process involving ACC hydration/dissolution and then dehydration/crystallization, aragonite fusion/growth, and calcite formation (Supplementary Fig. S6). Such a concrete-like quick consolidation behavior and a porous structure will ensure $mCaCO_3$ to weld polymer chains occluded within the mesoporous channels.

3.2. Synthesis and microstructure characterization of $mCaCO_3$-PHBV membrane

Next, PHBV was chosen as a model polymer to construct wound dressing with $mCaCO_3$ nanoconcretes together because PHBV has excellent biodegradation and high biocompatibility but relatively low toughness [38]. A freeze-drying method was developed to quickly crystallize the solvent dichloromethane (DCM) and PHBV under cooling of liquid nitrogen, and then to form the $mCaCO_3$-encapsulated PHBV membrane with porous structure after quick sublimation/removal of DCM crystals under vacuum (Fig. 2b) [39,40]. Then the $mCaCO_3$-encapsulated PHBV membrane was immersed into water to locally crystallize $mCaCO_3$ nanoconcretes into calcite nanocrystals in a confined space, which occluded and welded the encapsulated chains of PHBV to form the $mCaCO_3$-welding PHBV membrane ($mCaCO_3$-PHBV) (Fig. 2b). As a control, the $sCaCO_3$-encapsulated PHBV membrane ($sCaCO_3$@PHBV) was also prepared by the same procedure. From TEM images of 60 nm-thick transverse section, both $mCaCO_3$-PHBV and $sCaCO_3$@PHBV exhibited high porosity with about 100 nm in diameter and high dispersion of calcite nanocrystals (Fig. 2b and Supplementary Fig. S7). Three-dimensional two-photon fluorescence imaging further discovered that pore channels were plentiful, oriented, aligned and opened (Fig. 2c and Supplementary Movie S1), which can be due to oriented and uniform crystallization of DCM under gradient cooling. Such a porous structure should be greatly favorable to improve hydrophilicity and water vapor permeability of PHBV membrane in imitation of partial skin functions. From high-resolution TEM images (Fig. 2de) and elementary mapping (Fig. 2f) of 60 nm-thick section of $mCaCO_3$-PHBV, PHBV chains were indeed incorporated into the crystal lattice of calcite nanocrystals as indicated by internal crystal deficiencies (yellow circles in Fig. 2de) and extra oxygen signal (Fig. 2f) outside of Ca (basically reflects oxygen in $CaCO_3$) within crystal where red without overlap with green belongs to occluded PHBV. By comparison, PHBV chains in the $sCaCO_3$@PHBV membrane only surrounded calcite nanocrystals rather than incorporated into their crystal lattice (Supplementary Fig. S8).

Supplementary data related to this article can be found at https://doi.org/10.1016/j.bioactmat.2021.12.014.

3.3. Mechanical performances and welding mechanisms of $mCaCO_3$-PHBV membrane

Furthermore, mechanical performances of membranes were evaluated from microscopic to macroscopic levels. At first, to detect the interfacial attractions between calcite nanocrystals and PHBV chains, the strain mappings across single $CaCO_3$ crystals in the 60 nm-thick slices of porous membranes were determined by geometric phase analysis (GPA). The percentage degrees of in-plane fringe deformation (ε_{xx}), out-of-plane fringe deformation (ε_{yy}), fringe rotation (R_{xy}), and shear strain (S_{xy}) were evaluated with respect to a reference area ($\varepsilon_{xx} = 0\%$, $\varepsilon_{yy} = 0\%$, $R_{xy} = 0°$, and $S_{xy} = 0\%$) arbitrarily selected in the nanocrystal center, and used to construct corresponding topological maps of strain distribution. In these maps, the color scale and the signs "+" and "-" denote, respectively, the extent and the direction of a particular strain component change, relative to the reference. From Fig. 3a, the ε_{xx}, ε_{yy}, R_{xy} and S_{xy} components in the $sCaCO_3$@PHBV sample generally exhibited weak oscillations which were discretely distributed in the nanocrystal, possibly owing to the formation of lattice fringe distortion during the concrete-like quick consolidation. By comparison, these components in the $mCaCO_3$-PHBV membrane sample displayed relatively stronger strains. Noticeably, the concerned fringes spanned the entire nanocrystal section in a continuous way, which should be attributed to the incorporation of polymer chains into calcite nanocrystal in accordance with the high-resolution TEM results in Fig. 2d–f. Therefore, it can be concluded that a strong strain of nanocrystal welding polymer chains was formed during the concrete-like quick consolidation. Such a microscopic nanocrystal-welding-polymer force would make a contribution to the macroscopic mechanical performances of $mCaCO_3$-PHBV membrane.

From Supplementary Fig. S9a, compared with the common natural drying method, the freeze-drying method can distinctly enhance the tensile strength and elongation of PHBV membrane, which can be attributed to quick freeze-drying-induced reduction in PHBV grain size as XRD peak width at half height decreased (Supplementary Fig. S10). The incorporation of $CaCO_3$ nanoparticles further decreased PHBV grain size (Supplementary Fig. S10) and thus freshly prepared $sCaCO_3$@PHBV membrane can mildly improve the tensile strength of PHBV membrane (1.3 fold, Supplementary Fig. S9). Besides PHBV crystallization,

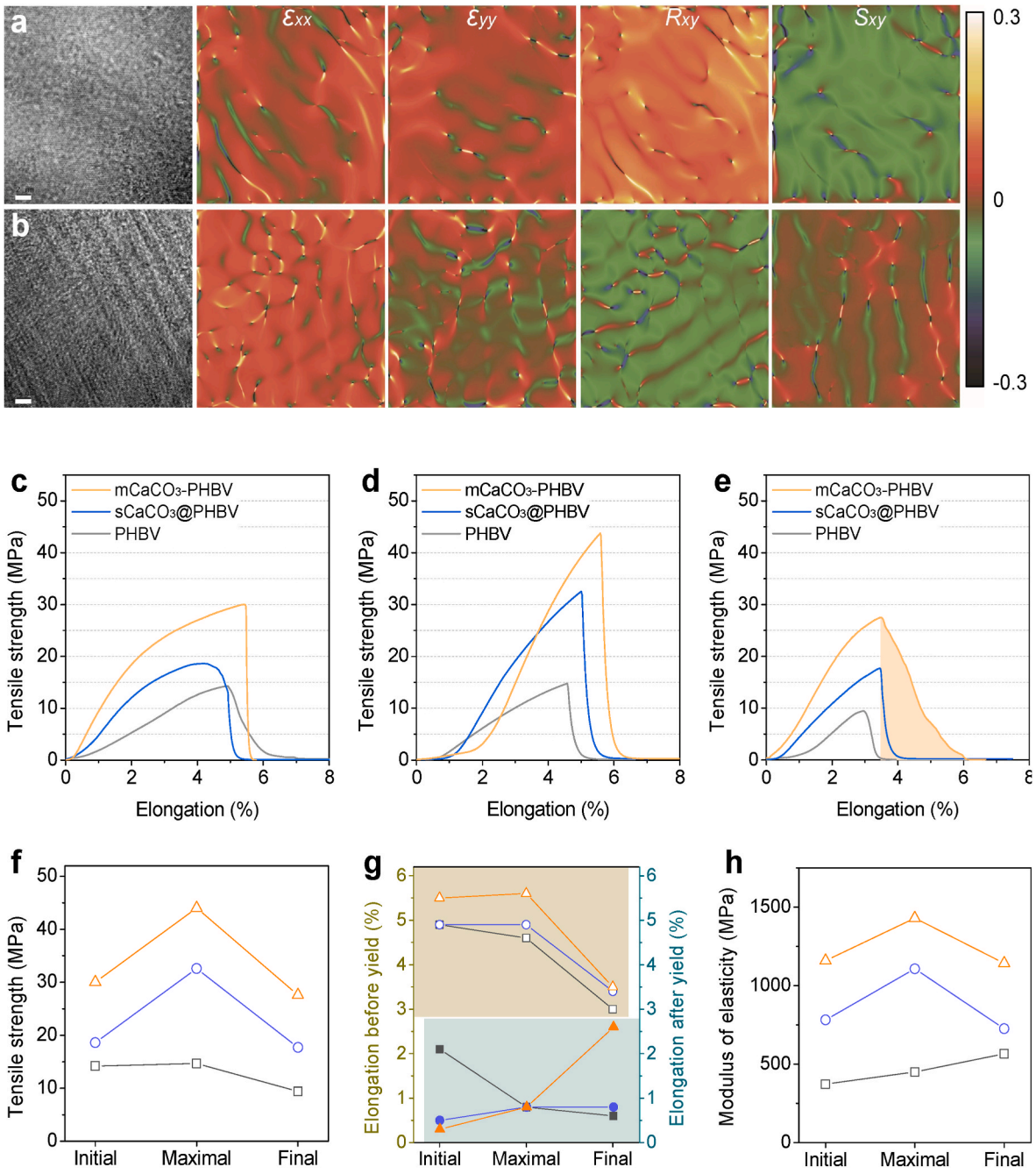

Fig. 3. Mechanical performances of porous membranes from microscopic stress and macroscopic strength. (**a**,**b**) High-resolution TEM and corresponding strain mappings for ε_{xx}, ε_{yy}, R_{xy}, and S_{xy} by GPA of $CaCO_3$ crystals in the 60 nm-thick slices of $sCaCO_3$@PHBV (**a**) and $mCaCO_3$-PHBV (**b**) membranes. Scale bar, 2 nm. (**c**–**e**) Tensile curves of porous membranes before bending (**c**), when achieving the maximal bending strength after bending (**d**), and after bending for 500 cycles (**e**). (**f**) Tensile strength of porous membranes before bending (Initial), when achieving the maximal bending strength after bending (Maximal), and after bending for 500 cycles (Final). (**g**) Elongations before and after yield of porous membranes. (**h**) Modulus of elasticity of porous membranes.

hydration-driven $mCaCO_3$ crystallization and PHBV welding made more remarkable contributions to both strengthening (2.1 fold) and toughening (Fig. 3c, Supplementary Fig. S9b–d) in accordance with GPA results.

Anti-fatigue performances were further evaluated by 500-cycle continuous bending (Supplementary Movie S2) since they are very important to tissue engineering, especially wound dressing. From Supplementary Fig. S11 and Fig. 4a, brittle fracture occurred in PHBV membrane after 99 cycles of bending, while it occurred in $sCaCO_3$@PHBV membrane after 352 cycles of bending. Strikingly, no brittle fracture was observed in $mCaCO_3$-PHBV membrane after bending strength began to attenuate at 268 cycles. To track the change in mechanical performances during bending, we collected data at three points, the initial point before bending (Fig. 3c), the maximal/critical point where bending strength arrived at the maximum (Fig. 3d), and the final point after 500 cycles of bending (Fig. 3e). It can be found that both tensile strength and elastic elongation of PHBV gradually decreased during the bending cycle, but that of $sCaCO_3$@PHBV membrane and $mCaCO_3$-PHBV membrane firstly increased and then decreased, and always followed the law of $mCaCO_3$-PHBV>$sCaCO_3$@PHBV>PHBV (Fig. 3g,h,i). Noticeably, elongation after yielding of $mCaCO_3$-PHBV membrane always increased during bending cycle (Fig. 3h) and became

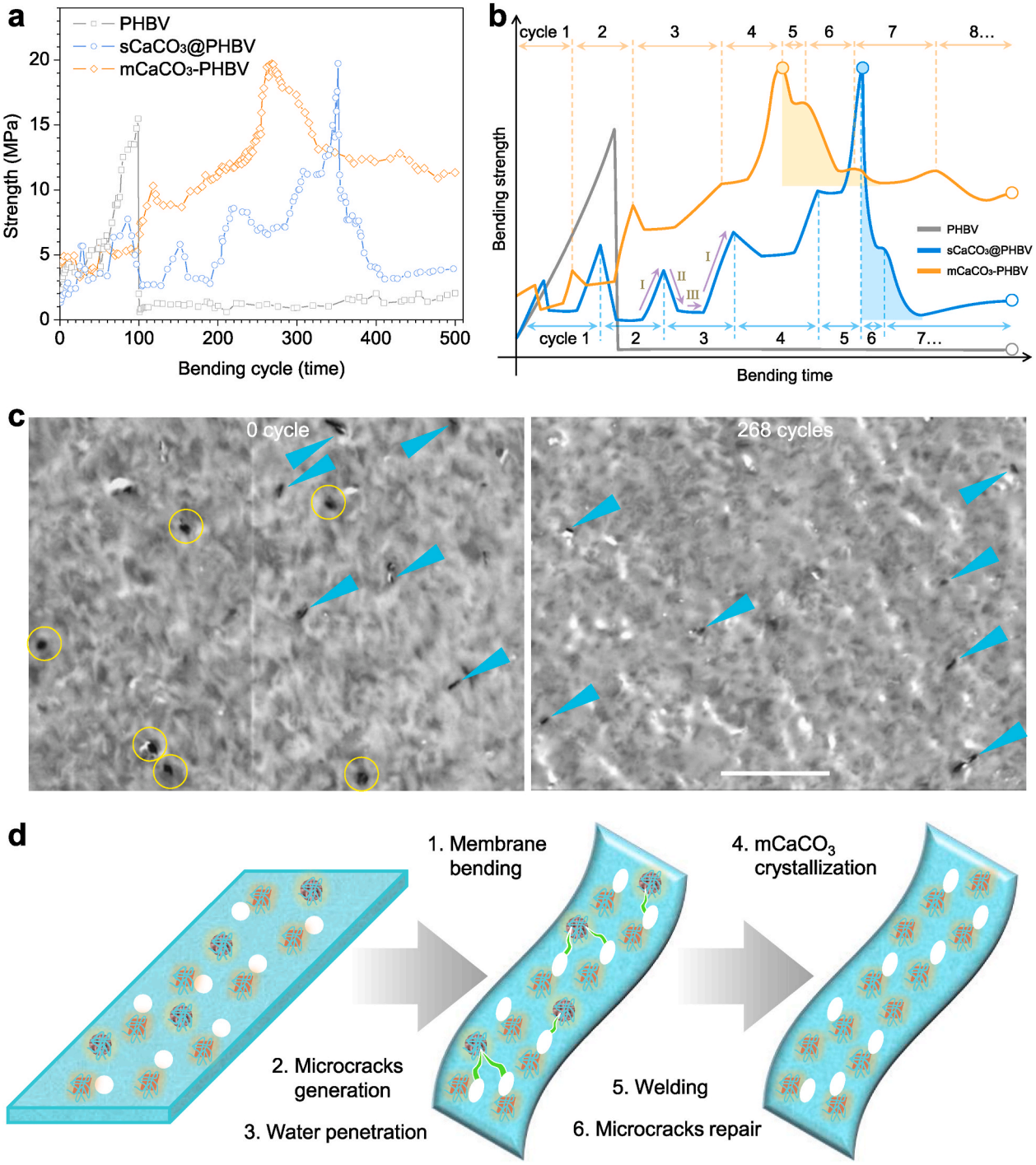

Fig. 4. Anti-fatigue performances and mechanisms of porous membranes. (**a**) Bending strength change of porous membranes during 500-cycle continuous bending. (**b**) Tendency charts extracted from Fig. 4a, where three steps included in each strength change cycle represent energy accumulation (I), energy release from microcracks (II), and energy absorption by nanoparticles (III). (**c**) STEM images of 60 nm-thick slices of $mCaCO_3$-PHBV membranes before bending and after bending for 268 cycles. Scale bar, 2 μm. Yellow circles and blue arrows represent non-crystallization and crystallization of $mCaCO_3$ nanoconcretes, respectively. (**d**) Schematic diagram of anti-fatigue mechanisms of $mCaCO_3$-PHBV membrane.

remarkably more than that of $sCaCO_3$@PHBV membrane after 500 cycles (orange shadow in Fig. 3g), indicating that bending $mCaCO_3$-PHBV membrane gradually enhanced its toughness and meanwhile maintained a relatively high strength, owing to powerful welding force. Such simultaneous strengthening, toughening and anti-fatigue effects are quite significant to realize high mechanical performances of wound dressing.

Supplementary data related to this article can be found at https://doi.org/10.1016/j.bioactmat.2021.12.014.

Moreover, in order to make clear the mechanism of strengthening, toughening and anti-fatigue effects, we further tracked and analyzed mechanical behaviors of membranes during bending cycles. From tendency charts in Fig. 4b extracted from original data in Fig. 4a, distinctly different from brittle fracture behavior of PHBV, $mCaCO_3$-PHBV and $sCaCO_3$@PHBV membranes experienced the cycles of transient generation and repair of microcracks, where there were three steps in each

cycle (purple arrows in Fig. 4b): Step I, energy accumulation; Step II, energy release from microcracks; Step III, energy absorption by nanoparticles. It is obvious that both $sCaCO_3$ and $mCaCO_3$ nanocrystals as a second phase effectively blocked the expansion of microcracks by absorbing their energy, increasing the toughness of PHBV membrane. Compared with $sCaCO_3$@PHBV membrane, $mCaCO_3$-PHBV membrane can more quickly (reflected by more cycle times, Fig. 4b) absorb higher energy (reflected by the area under the curve, Fig. 4b), more efficiently enhancing the toughness. It should originate from a stronger interfacial binding force between $mCaCO_3$ nanocrystal and PHBV chains. In addition, after elastic yield, $mCaCO_3$-PHBV membrane exhibited higher plasticity than $sCaCO_3$@PHBV membrane, as suggested by bigger area of shadow under the curve in Fig. 4b (orange versus blue), and also maintained remarkably higher strengths than $sCaCO_3$@PHBV membrane.

Noticeably, elongation after yielding of $mCaCO_3$-PHBV membrane always increased during bending cycle (Fig. 3g) and became remarkably more than that of $sCaCO_3$@PHBV membrane after 500 cycles (orange shadow in Fig. 3g), indicating that bending $mCaCO_3$-PHBV membrane gradually enhanced its toughness and meanwhile maintained a relatively high strength, owing to powerful welding force. Such simultaneous strengthening, toughening and anti-fatigue effects are quite significant to realize high mechanical performances of wound dressing. Moreover, before yielding (Fig. 4b), the difference of strength between $mCaCO_3$-PHBV and $sCaCO_3$@PHBV membrane overall became bigger and bigger with the increase of energy-absorption cycle (Supplementary Fig. S12), suggesting that there was another factor besides bending-induced polymer hardening making a contribution to the strengthening of $mCaCO_3$-PHBV membrane during bending. Therefore, we further checked the microstructure of $mCaCO_3$-PHBV membrane at the

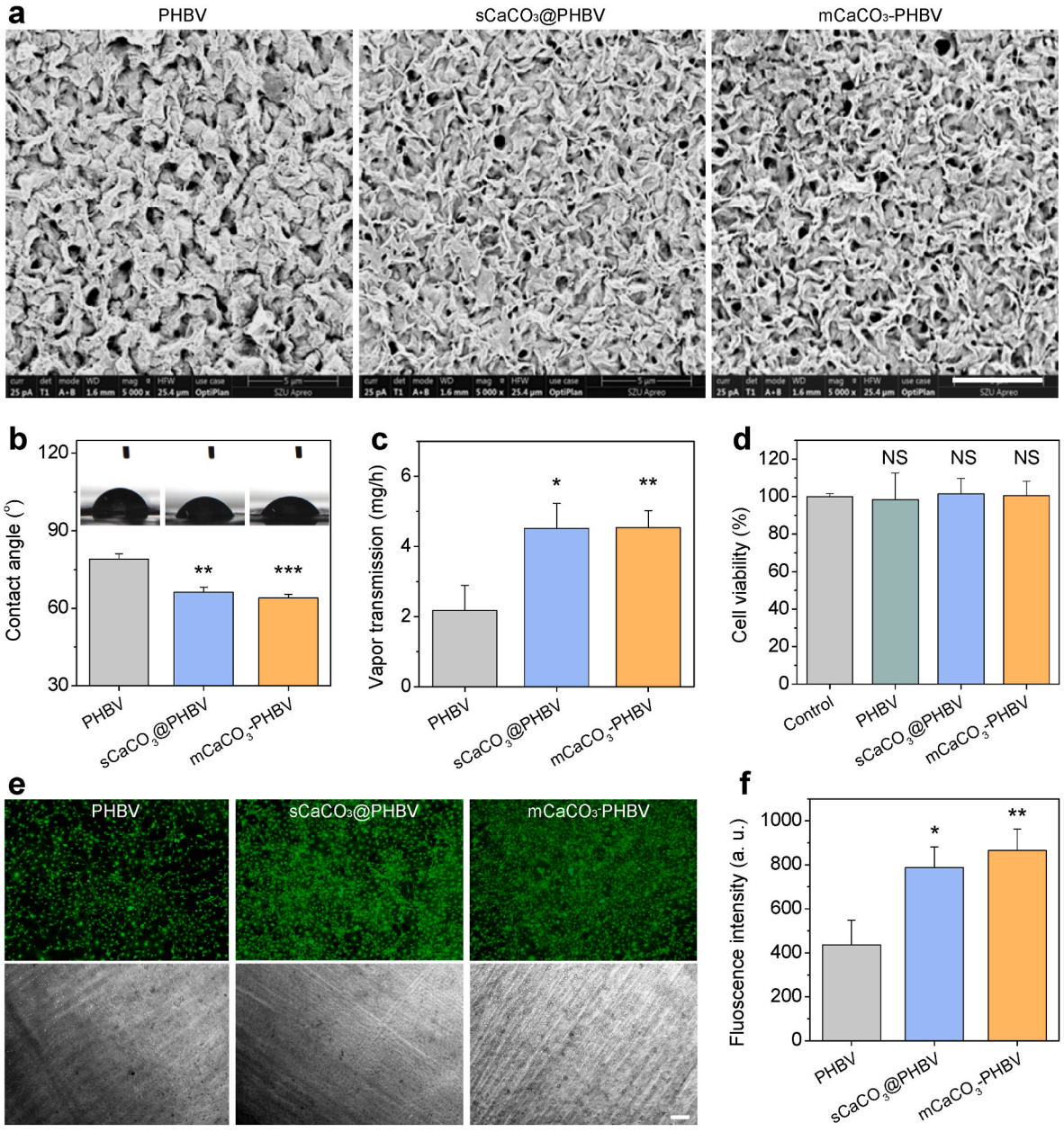

Fig. 5. Biological performances of porous membranes. (**a**) Surface topography (Scale bar, 5 μm), (**b**) Hydrophilicity, (**c**) Water vapor permeability, (**d**) Cytotoxicity to 3T3 cells, (**e**) fluorescence images of 3T3 cell adherence and proliferation on PHBV, $sCaCO_3$@PHBV and $mCaCO_3$-PHBV membranes (Scale bar, 100 μm), and (**f**) Corresponding quantitative analysis. *P* values were calculated by the two-tailed Student's *t*-test (*$p < 0.05$, **$p < 0.01$, ***$p < 0.0001$; NS, no significant difference).

critical yield point. We found that there were partial $mCaCO_3$ nanoconcretes away from PHBV pores not crystallized yet (as indicated by yellow circles in Fig. 4c), but they became crystalline after 268-cycle bending (as indicated by blue arrows in Fig. 4c). We think that it resulted from microcracks-induced penetration of water from PHBV pores to $mCaCO_3$ nanoconcretes and subsequent hydration-induced $mCaCO_3$ crystallization and welding with PHBV (Fig. 4d). The case of $sCaCO_3$@PHBV membrane was similar (Supplementary Fig. S13). In this period, the energy of microcracks can not only be absorbed by $mCaCO_3$ nanoconcretes, but also induce their crystallization/welding to repair microcracks for strengthening. Such a bending-driven strengthening and toughening effect is quite interesting and unexpected in great favor of the clinical application of wound dressing.

3.4. *Biological performances of $mCaCO_3$-PHBV membrane as wound dressing*

Biological performances of $mCaCO_3$-PHBV membrane, including hydrophilicity, gas transmission, cell adherence and anti-bacterial were explored. Surface microstructure/topography is a very important factor influencing these performances. From Fig. 5a, PHBV, $sCaCO_3$@PHBV and $mCaCO_3$-PHBV membranes exhibited a kind of rough and porous surface with nanoplates-constructed microstructure, and the surface roughness of PHBV membrane was higher than that of $sCaCO_3$@PHBV and $mCaCO_3$-PHBV membranes owing to bigger PHBV grain size (Supplementary Fig. S10b). Nanoplate morphology suggested oriented growth of PHBV crystals in accordance with XRD results (Supplementary Fig. S10a). Different from general PHBV materials with high hydrophobicity (contact angle of about 129°) [41], PHBV membrane in this work exhibited a remarkably lower contact angle of 79° (Fig. 5b), possibly owing to the porous structure and rough nano-/micro-structure. Compared PHBV membrane, $sCaCO_3$@PHBV and $mCaCO_3$-PHBV membranes displayed a lower contact angle (Fig. 5b), which could be attributed to $CaCO_3$ incorporation, demonstrating higher hydrophilicity in support of water vapor transmission (Fig. 5c). Moreover, PHBV, $sCaCO_3$@PHBV and $mCaCO_3$-PHBV membranes had no visible cytotoxicity to both 3T3 fibroblast cells (Fig. 5d) and MCF-10A endothelial cells (Supplementary Fig. S14). $mCaCO_3$-PHBV membrane can best induce the adherence (Supplementary Fig. S15) and proliferation (Fig. 5ef) of 3T3 fibroblast cells compared with PHBV and $sCaCO_3$@PHBV membrane, owing to its highest hydrophilicity and fine surface nano-/micro-structure [42]. The order stripes of the membrane in the bright field images in Fig. 5e, which were derived from the surface structure of model, were on the opposite side of cellular adhesion, and

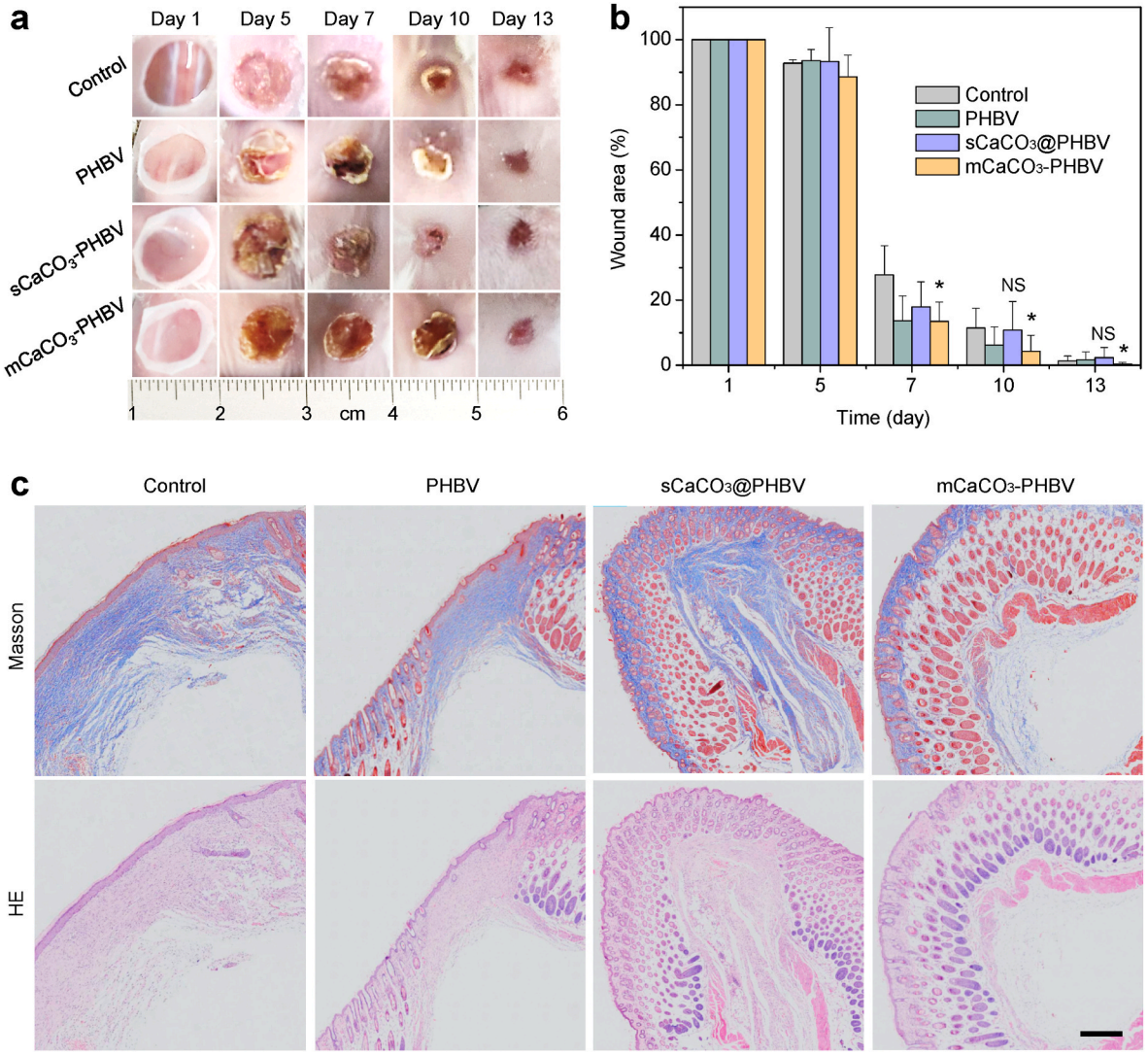

Fig. 6. ***In vivo*** **wound therapy effect of porous membranes as wound dressing.** (**a**) Photographs of wounds treated for 1, 5, 7, 10 and 13 days, (**b**) wound area during treatment, and (**c**) vertical section of healed skin at the center of wound stained by H&E and Masson methods (scale bar, 500 μm). *P* values were calculated by the two-tailed Student's *t*-test (*$p < 0.05$; NS, no significant difference).

therefore could not cause the orientation growth of cells as indicated by the fluorescence images in Fig. 5e. In addition, PHBV had a moderate anti-bacterial ability [43], and mCaCO$_3$-PHBV membrane exhibited a better anti-bacterial effect against *Escherichia coli* and *Staphylococcus aureus* (Supplementary Fig. S16), which possibly resulted from its specific nanoplate morphology [44,45].

Moreover, wound-healing performances of mCaCO$_3$-PHBV membrane as wound dressing were investigated using a wound model of mice. From Fig. 6a and b, mCaCO$_3$-PHBV membrane can accelerate wound healing faster compared with blank control. The mCaCO$_3$-PHBV membrane maintained higher integrity during the whole therapy period compared with PHBV and sCaCO$_3$@PHBV membranes (Fig. 6a), owing to its higher mechanical performances, in favor of more effectively blocking the invasion of bacteria and inducing the adherence and growth of cells. Although wounds in all treatment groups healed up finally, histopathologic examination of sections in the middle of wounds indicated that blank control caused severe fibrosis with rarely visible skin appendage, PHBV group still exhibited partial fibrosis, sCaCO$_3$@PHBV group repaired wound to a certain extent without obvious skin appendage, while mCaCO$_3$-PHBV membrane induced the full growth of epidermis, hypodermis and skin appendage with plentiful hair follicles, glandular integumentaria and clear blood vessels (Fig. 6c). Therefore, mCaCO$_3$-PHBV membrane can effectively improve wound healing by inducing the integrated adherence and substantial growth of functional cells because of high hydrophilicity and roughness rather than by causing fibrosis, and thus mCaCO$_3$-PHBV-repairing wound will have better biological functions of the skin. In addition, mCaCO$_3$-PHBV membrane exhibited high blood compatibility and invisible toxicity to main normal organs (Supplementary Fig. S17−19).

4. Conclusion

In summary, we developed an ion etching method to synthesize a kind of mesoporous CaCO$_3$ nanoconcretes composed of amorphous and nanocrystalline phases, and utilized them to construct a type of porous organic/inorganic membrane by a freeze-drying/hydration method. The polymer welding effect of mesoporous CaCO$_3$ nanoconcretes was confirmed to play a primary role in strengthening and toughening the porous PHBV membrane. Mechanical and biological performances were improved by the welding strategy, and the constructed mCaCO$_3$-PHBV membrane was used as wound dressing, exhibiting ideal wound repair outcomes. The proposed nanoconcrete-welding-polymer concept delivers a promising strategy for improving the mechanical performances of polymers. In principle, this is a general platform technology which is possibly extendable to be applied in various macromolecular matrices.

CRediT authorship contribution statement

Yingshuai Wang: conducted the experiments, analyzed the data, and wrote the manuscript, Formal analysis, Writing – original draft. **Yanxia Zhu:** conducted the experiments, analyzed the data, and revised the manuscript, Formal analysis, Writing – original draft. **Penghe Zhao:** provided suggestions for experiments and helped with some of the experiments. **Bin Wei:** provided help for TEM measurement. **Mingjian Fan:** did SEM measurement. **Danyang Chen:** provided help with some of the experiments. **Zhaokui Jin:** provided help and suggestions for experiments. **Qianjun He:** conceived the project idea, supervised the project, conducted the partial experiments, helped with data analysis and revised the manuscript, Formal analysis, Writing – original draft, Supervision.

Declaration of competing interest

The authors declare no conflicts of interest regarding the publication of this paper.

Acknowledgements

We greatly appreciate the inspiration and guidance of Prof. Meldrum C. Fiona (UoL) in calcium carbonate biomineralization, the discussion with Prof. Junhong Lv (SIAP CAS) in microstructure measurement, the help of Dr. Heliang Yao (SIC CAS) for TEM measurement, the assistance of Dr. Chenyang Wei (SIC CAS) in XRD and BET measurements, and the Instrumental Analysis Center of Shenzhen University (XiLi campus) for assistance in material characterizations. This work was supported by the National Natural Science Foundation of China (51872188), Shenzhen Basic Research Program (SGDX20201103093600004), Special Funds for the Development of Strategic Emerging Industries in Shenzhen (20180309154519685), SZU Top Ranking Project (860-00000210), the PhD Start-up Fund of Natural Science Foundation of Guangdong Province (2018A030310573, 2021A1515011155), China Postdoctoral Science Foundation (2018M643171), and Center of Hydrogen Science, Shanghai Jiao Tong University, China.

Appendix A. Supplementary data

Supplementary data to this article can be found online at https://doi.org/10.1016/j.bioactmat.2021.12.014.

References

[1] M.J. Webber, E.A. Appel, E.W. Meijer, Supramolecular biomaterials, Nat. Mater. 15 (2016) 13–26.
[2] K. Rezwan, Q.Z. Chen, J.J. Blaker, A.R. Boccaccini, Biodegradable and bioactive porous polymer/inorganic composite scaffolds for bone tissue engineering, Biomaterials 27 (2006) 3413–3431.
[3] E. Ma, X. Wu, Tailoring heterogeneities in high-entropy alloys to promote strength–ductility synergy, Nat. Commun. 10 (2019) 5623.
[4] X. Li, W. Liu, L. Sun, Y. Fan, Q. Feng, The application of inorganic nanomaterials in bone tissue engineering, J. Biomater. Tiss. Eng. 4 (2014) 994–1003.
[5] P. Song, Z. Xu, M.S. Dargusch, Z.G. Chen, H. Wang, Q. Guo, Granular nanostructure: a facile biomimetic strategy for the design of supertough polymeric materials with high ductility and strength, Adv. Mater. 29 (2017), 1704661.
[6] N. Domun, H. Hadavinia, T. Zhang, T. Sainsbury, S. Vahid, Improving fracture toughness and strength of epoxy using nanomaterials – a review of current status, Nanoscale 7 (2015) 10294–10329.
[7] P. Fratzl, H.S. Gupta, E.P. Paschalis, P. Roschger, Structure and mechanical quality of the collagen-mineral nano-composite in bone, J. Mater. Chem. 14 (2004) 2115–2123.
[8] J. Yao, H. Hu, Z. Sun, Y. Wang, H. Huang, L. Gao, X. Jiang, X. Wang, C. Xiong, Synchronously strengthen and toughen polypropylene using tartaric acid-modified nano-CaCO$_3$, Nanomaterials 11 (2021) 2493.
[9] M. Catauro, E. Tranquillo, G.D. Poggetto, S. Naviglio, F. Barrino, Antibacterial properties of Sol–Gel biomaterials with different percentages of PEG or PCL, Macromol. Symp. 389 (2020), 1900056.
[10] L. Yang, H. Yang, W. Hao, Y. Li, Q. Li, T. Sun, Fabrication, characterization and antibacterial mechanism of in-situ modification nano-CaCO$_3$/TiO$_2$/CS coatings, Int. J. Food Sci. Technol. 56 (2021) 2675.
[11] X. Ge, C. Ren, Y. Ding, G. Chen, X. Lu, K. Wang, F. Reng, M. Yang, Z. Wang, J. Li, X. An, B. Qian, Y. Leng, Micro/nano-structured TiO$_2$ surface with dual-functional antibacterial effects for biomedical applications, Bioact. Mater. 4 (2019) 346.
[12] S. Kirboga, M. Ner, Oxygen barrier and thermomechanical properties of poly (3-hydroxybutyrate-*co*-3-hydroxyvalerate) biocomposites reinforced with calcium carbonate particles, Acta Chim. Slov. 67 (2020) 137–150.
[13] C.M. Chan, J. Wu, J.X. Li, Y.K. Cheung, Polypropylene/calcium carbonate nanocomposites, Polymer 43 (2002) 2981–2992.
[14] Z. Mu, K. Kong, K. Jiang, H. Dong, X. Xu, Z. Liu, R. Tang, Pressure-driven fusion of amorphous particles into integrated monoliths, Science 372 (2021) 5277.
[15] Y. He, K. Kong, Z. Guo, W. Fang, Z. Ma, H. Pan, R. Tang, Z. Liu, A highly sensitive, reversible, and bidirectional humidity actuator by calcium carbonate ionic oligomers incorporated poly(vinylidene fluoride), Adv. Funct. Mater. 31 (2021), 2101291.
[16] K. Li, D. Li, L. Zhao, Y. Chang, Y. Zhang, Y. Cui, Z. Zhang, Calcium-mineralized polypeptide nanoparticle for intracellular drug delivery in osteosarcoma chemotherapy, Bioact. Mater. 5 (2020) 721.
[17] Z. Liu, C. Shao, B. Jin, Z. Zhang, R. Tang, Crosslinking ionic oligomers as conformable precursors to calcium carbonate, Nature 574 (2019) 394–398.
[18] Y.Y. Kim, K. Ganesan, P. Yang, A.N. Kulak, S. Borukhin, S. Pechook, L. Ribeiro, R. Kröger, S.J. Eichhorn, S.P. Armes, B. Pokroy, F.C. Meldrum, An artificial biomineral formed by incorporation of copolymer micelles in calcite crystals, Nat. Mater. 10 (2011) 890–896.
[19] C.K. Rae, Y.Y. Kim, P. Yang, W. Cai, H. Pan, A.N. Kulak, J.L. Lau, P. Kulshreshtha, S.P. Armes, F.C. Meldrum, J.J. De Yoreo, Direct observation of mineral–organic

composite formation reveals occlusion mechanism, Nat. Commun. 7 (2016), 10187.
[20] D.C. Green, M.A. Holden, M.A. Levenstein, S. Zhang, B.R.G. Johnson, G.D.P. Julia, A. Ward, S.W. Botchway, F.C. Meldrum, Controlling the fluorescence and room-temperature phosphorescence behaviour of carbon nanodots with inorganic crystalline nanocomposites, Nat. Commun. 10 (2019) 206.
[21] Y.Y. Kim, R. Darkins, A. Broad, A.N. Kulak, F.C. Meldrum, Hydroxyl-rich macromolecules enable the bio-inspired synthesis of single crystal nanocomposites, Nat. Commun. 10 (2019) 5682.
[22] Y. Kim, J. Carloni, B. Demarchi, Tuning hardness in calcite by incorporation of amino acids, Nat. Mater. 15 (2016) 903–910.
[23] D.C. Green, J. Ihli, P.D. Thornton, M.A. Holden, B. Marzec, Y.Y. Kim, A.N. Kulak, M.A. Levenstein, C. Tang, C. Lynch, S.E.D. Webb, C.J. Tynan, F.C. Meldrum, 3D visualization of additive occlusion and tunable full-spectrum fluorescence in calcite, Nat. Commun. 7 (2016), 13524.
[24] C.C. Xue, M.H. Li, Y. Zhao, Tumor microenvironment-activatable Fe-doxorubicin preloaded amorphous $CaCO_3$ nanoformulation triggers ferroptosis in target tumor cells, Sci. Adv. 6 (2020), eaax1346.
[25] N. Yin, A.F. Lee, P.D.R. Liam, Y.W. Wang, F.C. Meldrum, P.A. Steven, Occlusion of sulfate-based diblock copolymer nanoparticles within calcite: effect of varying the surface density of anionic stabilizer chains, J. Am. Chem. Soc. 138 (2016) 11734–11742.
[26] J.Y. Kohno, F. Mafuné, T. Kondow, T. Formation of $Ca^{+}(EtOH)_m$ from alcohol solutions of $CaCl_2$, J. Phys. Chem. A 104 (2000) 1079–1084.
[27] S.F. Chen, H. Cölfen, M. Antonietti, S.H. Yu, Ethanol assisted synthesis of pure and stable amorphous calcium carbonate nanoparticles, Chem. Commun. 49 (2013) 9564–9566.
[28] Z. Dong, Synthesis of hollow biomineralized $CaCO_3$–polydopamine nanoparticles for multimodal imaging-guided cancer photodynamic therapy with reduced skin photosensitivity, J. Am. Chem. Soc. 140 (2018) 2165–2178.
[29] X. Liu, L. Zhang, Y. Wang, C. Guo, E. Wang, Biomimetic crystallization of unusual macroporous calcium carbonate spherules in the presence of phosphatidylglycerol vesicles, Cryst. Growth Des. 8 (2008) 759–762.
[30] S. Sun, D. Gebauer, H. Cölfen, A general strategy for colloidal stable ultrasmall amorphous mineral clusters in organic solvents, Chem. Sci. 8 (2017) 1400–1405.
[31] G. Magnabosco, I. Polishchuk, B. Pokroy, R. Rosenberg, H. Cölfen, G. Falini, Synthesis of calcium carbonate in trace water environments, Chem. Commun. 53 (2017) 4811–4814.
[32] K. Simkiss, Phosphates as crystal poisons in calcification, BioI. Rev. 39 (1964) 487–505.
[33] R.F. Reitemeier, T.F. Buehrer, The inhibiting action of minute amounts of sodium hexametaphosphate on the precipitation of calcium carbonate from ammoniacal solutions. i. quantitative studies of the inhibition process, J. Phys. Chem. B 44 (1940) 535–551.
[34] T.F. Buehrer, R.F. Reitemeier, The inhibitory action of minute amounts of sodium hexametaphosphate on the precipitation of calcium carbonate from ammoniacal solutions. II. Mechanism of the process with special reference to the formation of calcium carbonate, J. Phys. Chem. 44 (5) (1940) 552–574.
[35] T. Mass, Amorphous calcium carbonate particles form coral skeletons, Proc. Natl. Acad. Sci. U. S. A. 114 (2017) E7670–E7678.
[36] C.Y. Wu, D. Young, J. Martel, J.D. Young, A story told by a single nanoparticle in the body fluid: demonstration of dissolution-reprecipitation of nanocrystals in a biological system, Nanomedicine 10 (2015) 2659–2676.
[37] C.I. Steefel, P.V. Cappellen, A new kinetic approach to modeling water-rock interaction: the role of nucleation, precursors, and ostwald ripening, Geochem. Cosmochim. Acta 54 (1990) 2657–2677.
[38] R.B. Ariagna, A. ángel Serrano, Poly(3-hydroxybutyrate-*co*-3-hydroxyvalerate): enhancement strategies for advanced applications, Polymers 10 (2018) 732.
[39] L. Qian, H. Zhang, Controlled freezing and freeze drying: a versatile route for porous and micro-/nano-structured materials, J. Chem. Technol. Biotechnol. 86 (2011) 172–184.
[40] L.-B. Mao, Synthetic nacre by predesigned matrix-directed mineralization, Science 354 (2016) 107–110.
[41] M. Kouhi, J.V. Reddy, M. Fathi, Poly(3-hydroxybutyrate-*co*-3-hydroxyvalerate)/fibrinogen/bredigite nanofibrous membranes and their integration with osteoblasts for guided bone regeneration, J. Biomed. Mater. Res. 107 (2019) 1154–1165.
[42] M. Jager, C. Zilkens, K. Zanger, R. Krauspe, Significance of nano- and microtopography for cell-surface interactions in orthopaedic implants, J. Biomed. Biotechnol. (2007), 69036, 2007.
[43] G.R. Saad, M.A. Elsawy, M.Z. Elsabee, Preparation, characterization and antimicrobial activity of poly(3-hydroxybutyrate-*co*-3-hydroxyvalerate)-*g*-poly(n-vinylpyrrolidone) copolymers, Polym-Plast. Technol. 51 (2012) 1113–1121.
[44] J. Hasan, S. Jain, R. Padmarajan, S. Purighalla, V.K. Sambandamurthy, K. Chatterjee, Multi-scale surface topography to minimize adherence and viability of nosocomial drug-resistant bacteria, Mater. Des. 140 (2018) 332–344.
[45] S.D. Puckett, E. Taylor, T. Raimondo, T.J. Webster, The relationship between the nanostructure of titanium surfaces and bacterial attachment, Biomaterials 31 (2010) 706–713.